Microscopy, 2026, **75(2)**, 157–163
https://doi.org/10.1093/jmicro/dfag007
Advance access publication 16 February 2026
Special Issue Paper

MICROSCOPY

Probing the effective mass and fermi velocity of charges by momentum-resolved electron energy loss spectroscopy

Chih-Ying Huang[1,2,†], Somboon Fongchaiya[1,3,4,5,†], Chen-Yu Hung[1,3,4,5,†], Ta-Lei Chou[1], Ssu-Yen Huang[2,6], Chao-Sung Lin[3,4,5], Chun-Wei Chen[3,4,5,6], Mason Klemm[7,8], Sijie Xu[7,8], Bin Gao[7,8], Pengcheng Dai[7,8] and Ming-Wen Chu[1,6,*]

[1]Center for Condensed Matter Sciences, National Taiwan University, 1, Sec. 4, Roosevelt Road, Taipei 10617, Taiwan
[2]Department of Physics, National Taiwan University, 1, Sec. 4, Roosevelt Road,Taipei 10617, Taiwan
[3]International Graduate Program of Molecular Science and Technology, National Taiwan University (NTU-MST), 1, Sec. 4, Roosevelt Road, Taipei 10617, Taiwan
[4]Molecular Science and Technology Program, Taiwan International Graduate Program (TIGP), Academia Sinica, 128, Sec. 2, Academia Road, Nankang, Taipei 11529, Taiwan
[5]Department of Materials Science and Engineering, National Taiwan University, 1, Sec. 4, Roosevelt Road, Taipei 10617, Taiwan
[6]Center of Atomic Initiative for New Materials, National Taiwan University, 1, Sec. 4, Roosevelt Road, Taipei 10617, Taiwan
[7]Department of Physics and Astronomy, Rice University, 6100, Main Street, Houston, TX 77005, United States
[8]Rice Laboratory for Emergent Magnetic Materials and Smalley-Curl Institute, Rice University, 6100, Main Street, Houston, TX 77005, United States

*To whom correspondence should be addressed. E-mail: chumingwen@ntu.edu.tw

†These authors contributed equally to this work.

Abstract

The effective mass (m^*) and Fermi velocity (v_F) are two fundamental gauges of the electronic properties of materials and conventionally measured by magnetotransport characterizations. In this Review, we introduce momentum(q)-resolved electron energy loss spectroscopy (q-EELS) as an alternative method for probing m^* and v_F, and demonstrate its applications in semiconductor Si and semimetal FeGe. The q-EELS methodology is based on the q-dependent plasmon dispersion in the context of the random-phase approximation (RPA) for a free-electron gas (FEG), featuring a quantitative dependence on m^* and v_F and thus providing the route for retrieving these parameters. We outline the experimental principles for characterizing plasmon dispersions from the optical light line (the order of 10^{-3} Å^{-1}) to Brillouin-zone boundaries (the order of Å^{-1}), and elucidate the theoretical framework for pertinent elaborations on m^* and v_F. This work provides both the conceptual and practical guidelines for employing the q-EELS to extract m^* and v_F of fundamental significances to electronic characteristics of matters.

Keywords: electron energy loss spectroscopy, momentum, effective mass, Fermi velocity, plasmon dispersion.

Introduction

EELS probes the electronic excitations in matters and is of the reflection and transmission types [1-6]. The reflection EELS is characteristically paired with slow electrons of few tens of eV, which mediate the meV energy resolution indispensable for tackling the low-energy excitations of phonons (collective motions of atoms in solids) and magnons (collective spin excitations) characteristically below 50 meV [1-4]. The transmission EELS is otherwise installed in a transmission electron microscopy (TEM) or scanning TEM (STEM) with fast electrons of 30∼200 keV, endowing the energy resolution of a few hundreds of meV eligible for accessing electronic excitations above 1 eV such as plasmons, interband transitions and core-level excitations [5, 6]. Modern monochromatic electron optics in transmission EELS advances to the meV energy resolution characteristic of reflection EELS and renders the breakthrough of spatially-resolved EELS investigations of phonons in combination with STEM [7]. In contrast, the reflection EELS is short of spatial resolution [1-3], of which the particular strength of transmission EELS can also be converted into q resolution upon the setup of parallel electron-beam optics [6]. This work focuses on the q-resolved transmission EELS for plasmons within the capability of our energy (∼0.54 eV) and q resolution (ultimately, ∼0.001 Å^{-1}) and, thanks to the forward scattering of the fast electrons at 200 keV herein, the access to a large q space from the light line to Brillouin-zone boundaries is achievable by the electron diffraction [6]. Hereinafter, EELS refers to transmission EELS.

In principle, the characteristic loss function of EELS is depicted by $\mathrm{Im}\left\{\frac{1}{\varepsilon(\omega,q)}\right\}$, namely the imaginary part of the inverse of the frequency (ω)- and q-dependent complex dielectric function of $\varepsilon(\omega,q)$ [5]. Conversely, plasmons are the dynamical charge oscillations in solids in response to external electromagnetic stimuli and emerge at $\varepsilon(\omega,q)=0$, which indicates that the oscillating charge densities concomitantly screen the external electric field [8, 9]. Accordingly, the loss function would manifest a divergence upon the plasmon onset at $\varepsilon(\omega,q)=0$ and EELS forms the prominent probe for this collective plasmon excitation of charges (ω_p) [5], with

Received: 8 September 2025. **Revised:** 16 January 2026. **Accepted:** 4 February 2026

$\omega_p = \sqrt{\frac{4\pi ne^2}{m^* \varepsilon_\infty}}$ (n, the charge density; e, the electron charge; ε_∞, the screening dielectric constant) [5, 8, 9]. Upon the transfer of q to plasmons, the RPA within the FEG framework delineates a quadratic q^2-dispersion of the plasmons [9] and stimulated timeless q-EELS efforts in 1960' and 1970' for verifying this dispersion phenomenon in not only FEG-like metals but graphite and semiconductors [10-15], with Ref. [5] being a thorough review on the robustness of the RPA dispersion across the designated materials and the current work needing not to be redundant. Instead, what has not been resolved concerns how to quantitatively derive the essential m^*, v_F, and also n underlining the ω_p and characteristic q^2 dispersion without a priori knowledge on these parameters of matters [6]. Our review tackles this essential problem by the theoretical overview on plasmon dispersions in RPA for m^*, v_F and n, the basics on inelastic electron scattering of q-EELS for plasmon dispersions (example, Al), and the quantitative q-EELS derivations for m^*, v_F and n by the plasmon dispersions in Si and FeGe. The q-EELS capturing of the two highly demanded electronic parameters of m^* and v_F [16, 17] is demonstrated and urges extensive examinations of the methodology across versatile materials.

Methods

q-EELS experiments were conducted on a field-emission TEM (FEI Tecnai) operated at 200 keV and equipped with a Gatan Image Filter 865 EELS spectrometer. The circular EELS-entrance aperture of either 1 or 2.5 mm in diameter was selected upon the intended q resolution. For resolving plasmon dispersions close to the light line, an optimal q resolution of $\sim 0.001\,\text{Å}^{-1}$ is crucial [18] and achieved by the Midgley method [19], by which we significantly raised the sample plane till the formation of a sharp diffraction pattern on the viewing screen (the breadth of the diffraction spots being of $\sim 0.001\,\text{Å}^{-1}$) and increased the corresponding diffraction projection length by optical magnifications. A sharp diffraction spot of this kind was placed at the edge of the 1-mm EELS aperture for direct q-EELS mapping of the plasmon dispersion close to the light line (Fig. 1), and the breadth of $\sim 0.001\,\text{Å}^{-1}$ corresponds to the q resolution in this experimental setup [18]. Using the energy-selection window of 2 eV, we also conducted the energy-filtered imaging of the diffraction spot at the designated plasmon excitations in order to unveil the characteristic inelastic electronic scattering in q space. To further reveal plasmon dispersions at larger q up to Brillouin-zone boundaries, a compromised q resolution at the order of $0.1\,\text{Å}^{-1}$ is more practical and was achieved by a short projection of the conventional selected-area electron diffraction (SAED) patterns, with the exploitation of a 2.5-mm EELS aperture to increase the collection efficiency of the weak spectra at large q (Figs. 2 and 3; spectral intensities decaying by q^{-2} in theory [5, 8, 9]). The Al sample in Fig. 1 was prepared from the Al foil using twin jet and the respective Si and FeGe samples in Figs. 2 and 3 were subject to the mechanical polishing and Ar-ion thinning. The Al foil and Si single crystal are commercially available and the growth of the FeGe single crystal has been published elsewhere [20-23].

Results and discussion

To elucidate on the plasmon dispersions for m^*, v_F and n, we start from the onset condition of $\varepsilon(\omega, q) = 0$ for plasmons, with $\varepsilon(\omega, q) = 1 - \frac{4\pi e^2}{\varepsilon_\infty q^2}\chi(\omega, q)$ where $\chi(\omega, q)$ is the electronic susceptibility [5, 8] and formulated by the Lindhard response function as expanded below in the RPA context [24], where k_F is the Fermi wave vector with $(3\pi^2 n)^{\frac{1}{3}}$.

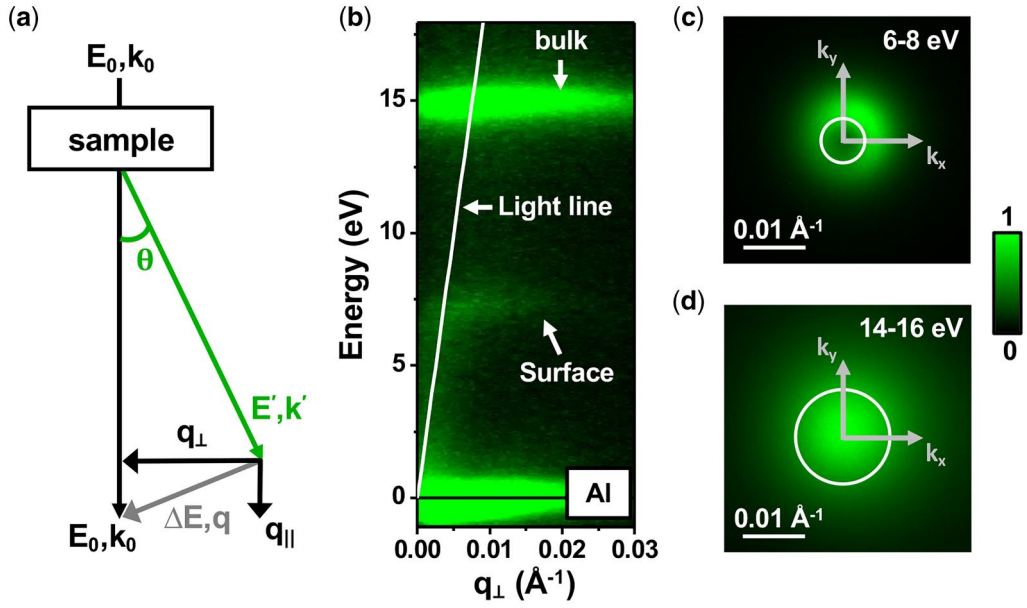

Fig. 1. (a) The inelastic electron scattering scheme of q-EELS. θ, the scattering angle. Details, see text. (b) The $\omega - q$ map of the bulk and surface plasmon dispersions in Al, with the light line being indicated by the white line. (c and d) The energy-filtered images of the transmitted spot in q space (denoted by k_x and k_y) with the 2-eV energy selection window centered at the surface and bulk plasmons, respectively. White circle in (c and d), the light cone. Color scale bar for (b–d), the normalized spectral intensity.

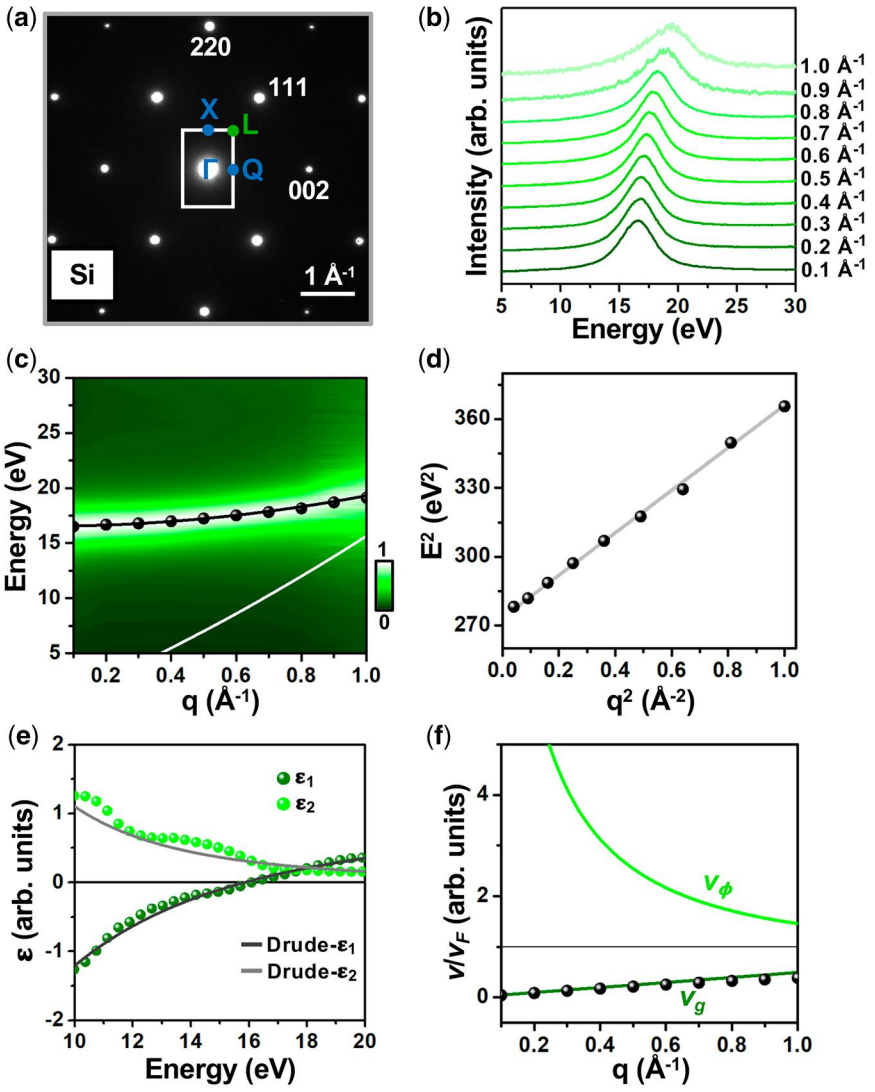

Fig. 2. (a) The first Brillouin zone in Si along the [1−10] projection. (b) The q-EELS spectra acquired along ΓL. (c) The $\omega - q$ map presentation of (b), with the spectral-intensity normalization to that at 0.1 Å^{-1} for revealing the weak plasmon at large q. Black dots, the plasmon peaks. Black curve, the calculated plasmon dispersion. White curve, the single-particularly continuum. Color scale bar, the normalized spectral intensity. (d) The $\omega^2 - q^2$ scaling of the plasmon peaks in (c). (e) The reported complex dielectric function of Si (light and dark green dots, the respective real and imaginary parts) [26]. The Drude-modelled real (black) and imaginary (gray) parts. (f) The calculated phase (v_ϕ; light green) and group (v_g; dark green) velocities of the plasmon normalized to the q-EELS derived v_F in Table 1. Black dots, the experimentally derived v_g from (c).

$$\chi(\omega,q) = \frac{4m^*k_F}{(2\pi\hbar)^2} \left\{\frac{1}{2} + \sum_{s=\pm1} \frac{1-(q/2k_F - s\omega/v_F q)^2}{4q/k_F} \ln\left(\frac{1+q/2k_F - s\omega/v_F q}{-1+q/2k_F - s\omega/v_F q}\right)\right\} \quad (1)$$

Solving Eq. (1) up to the sixth order of the natural-logarithm term in the Taylor series, one obtains $\varepsilon(\omega,q)$ in the following.

$$\varepsilon(\omega,q) = 1 - \frac{4\pi e^2}{\varepsilon_\infty q^2}\left\{\frac{nq^2}{m^*\omega^2} + \frac{3}{5}\frac{nv_F^2q^4}{m^*\omega^4}\right\} \quad (2)$$

Equation (3) is the solution of Eq. (2) in $\varepsilon(\omega,q) = 0$ [5, 8, 9] and sets the theoretical tone of this work.

$$\omega^2 = \omega_p^2 + \frac{3}{5}v_F^2q^2 \quad (3)$$

Taking the square root of Eq. (3) leads to the celebrated quadratic dispersion of plasmons in Eq. (4) [5, 8, 9].

$$\omega = \omega_p + \frac{3}{10}\frac{v_F^2q^2}{\omega_p} \quad (4)$$

Notably, the slope, A, in Eq. (3) upon the $\omega^2 - q^2$ scaling is a gauge of v_F by $A = \frac{3}{5}v_F^2$ provided a linearity is obeyed in the dispersion scaling (namely, the material being FEG-like) [6]. The ω_p formulation is then rewritten in $m^* = \frac{4\pi ne^2}{\omega_p^2\varepsilon_\infty}$, with which the A of $\frac{3}{5}v_F^2$ $\left(v_F = \frac{\hbar(3\pi^2n)^{\frac{1}{3}}}{m^*}\right)$ can be recast and subsequent straightforward mathematics yield the solution of n in Eq. (5) in Gaussian units.

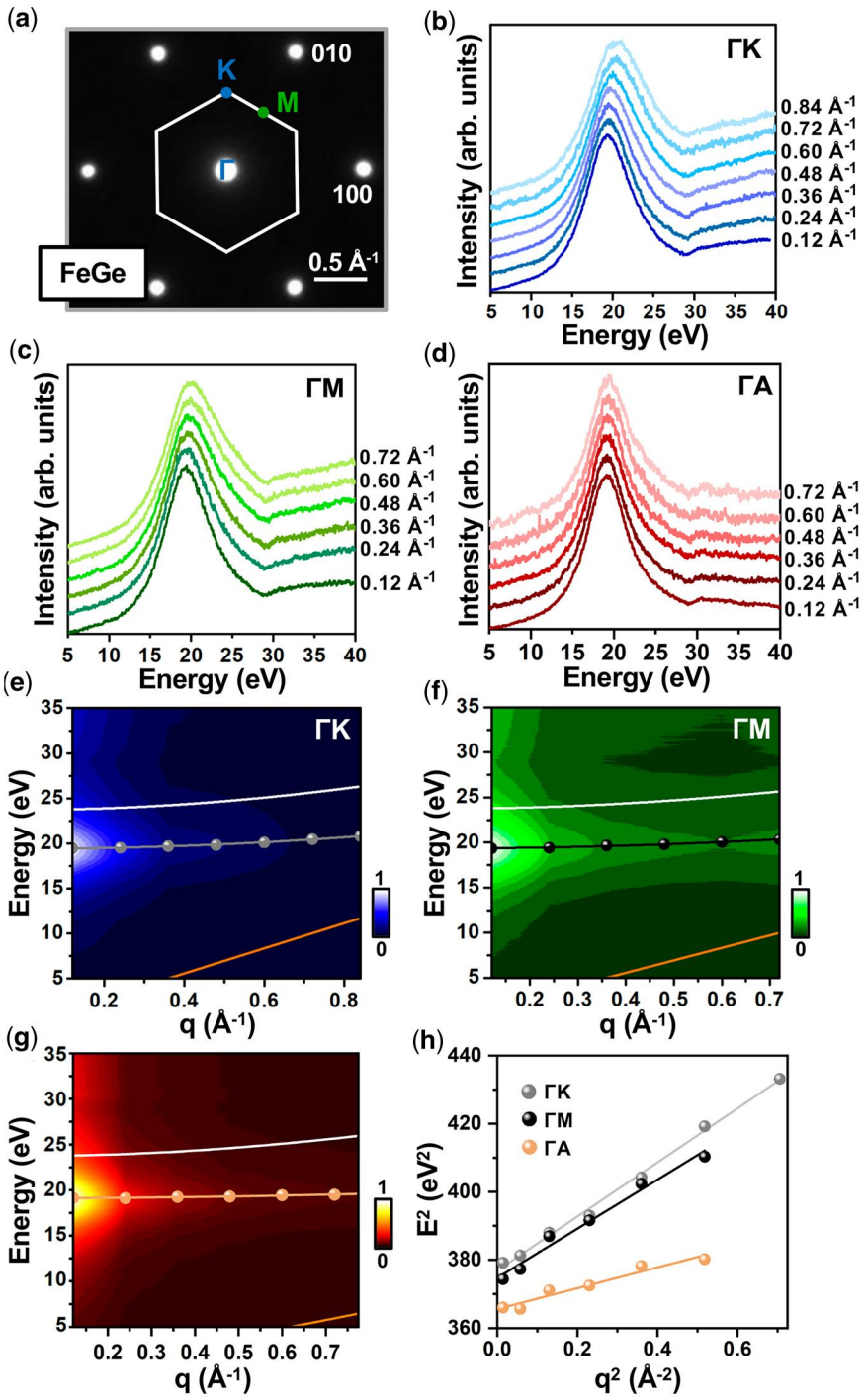

Fig. 3. (a) The first Brillouin zone in FeGe along the [001] projection. (b–d) The respective q-EELS spectra acquired along ΓK, ΓM and the out-of-plane ΓA. (e–g) The respective $\omega - q$ map presentations of (b–d). Gray, black and light-orange dots in respective (e–g), the plasmon peak positions. Gray, black and light-orange curves in respective (e–g), the calculated plasmon dispersions based on the q-EELS derived n, m^* and v_F. White curve in (e–g), the calculated plasmon dispersion based on the nominal n_0, m_0 and v_F. Orange curves in (e–g), the respective calculated single-particularly continua. Color scale bar, the spectral intensity. (h) The $\omega^2 - q^2$ scaling of the plasmon peaks along ΓK, ΓM and ΓA.

$$n = 1.524 \times 10^{21} \frac{(\hbar\omega_p)^3 \varepsilon_\infty^{\frac{3}{2}}}{A^{\frac{3}{4}}}, \mathrm{cm}^{-3} \qquad (5)$$

By Eq. (5), the n can be experimentally derived and one can then further resolve the associated m^* through the formulation of ω_p and v_F [6]. It is by far noticed that ε_∞ is crucial to this methodology of q-EELS probing of plasmon dispersions for m^*, v_F and n, and its estimation is exemplified in the later q-EELS study of Si. Now, we elucidate the experimental q-EELS principles using Al.

Figure 1a shows the inelastic scattering scheme of q-EELS, with the incident electron beam of the kinetic energy of E_0 and wave vector of k_0 ($k_0 = 2\pi/\lambda$; the present case of 200 keV, $\lambda = 0.0251$ Å). The significant k_0 mediates the characteristic forward scattering of electrons, with the midpoint between the corresponding Bragg-diffraction spots

Table 1. The nominal and q-EELS derived physical parameters of the valence electrons in Si and FeGe[a]

Material	Method	$\hbar\omega_p$ (eV)	n (n_0[b])	m^* (m_0[c])	v_F (cm/s)	k_F (Å^{-1})
Si	Nominal	16.6	1	1	2.09×10^8	1.81
	q-EELS, ΓL	16.6	1.16	1.17	1.88×10^8	1.90
FeGe	Nominal	23.8	1	1	2.66×10^8	2.30
	q-EELS, ΓK	19.5	1.03	1.54	1.74×10^8	2.32
	q-EELS, ΓM	19.3	1.03	1.55	1.73×10^8	2.32
	q-EELS, ΓA	19.1	1	2.46	1.08×10^8	2.30

a Standard errors in all evaluated parameters, ±10% (not shown for brevity) as determined by those in the ω^2-q^2 fitting to the plasmon-dispersion Eq. (3).
b n_0, the nominal valence-electron density, with 2×10^{23} cm^{-3} for Si and 4.1×10^{23} cm^{-3} for FeGe.
c m_0, the rest mass of electrons.

designating the Brillouin-zone boundary along a given symmetry direction (termed as the large-q regime) and the close vicinity to the transmitted electron beam underlining the light-line neighborhood (the small-q regime). The schematic Fig. 1a is valid to both large- and small-q inelastic scattering of E′ and k′, which transfers the energy △E and q to the materials for exciting plasmons of our central interest [5]. Specifically, the q is the vectorial sum of $q_\parallel$ and $q_\perp$, with $q=\sqrt{q_\parallel^2+q_\perp^2}$, $q_\parallel=k_0\frac{\Delta E}{2E_0}$ and $q_\perp$ being the arbitrary vector between the incident beam and zone boundary [5]. Considering the characteristically small inelastic-scattering angle of $\frac{\Delta E}{2E_0}$ of plasmons typically below 30 eV, $q_\parallel$ would be much smaller than $q_\perp$ in the q-EELS probing of plasmon dispersions, resulting in $q\approx q_\perp$. Figure 1b shows the $\omega-q$ mapping of the plasmon dispersions in Al using the Midgley method for q-EELS and the q axis is expressed in $q_\perp$ for highlighting the essence of $q\approx q_\perp$ in the current plasmon-energy scale. All $q_\perp$ hereinafter is denoted by q for brevity.

In Fig. 1b, the light line of $\omega=ck$ (c, the speed of light; k, the optical wave vector) crosses the bulk-ω_p plasmon at 15 eV and the surface-ω_s plasmon appears at ∼7 eV, with $\omega_s=\frac{\omega_p}{\sqrt{\varepsilon+\varepsilon_s}}$ where ε_s is the dielectric constant of the surface oxide overlayer on Al [5, 15]. The term of bulk is solely used here and the pertinent figure caption to differentiate from the surface contribution. Otherwise, plasmons in this work consistently refer to bulk plasmons, which are the oscillations of valence electrons [5, 8, 9]. The intense ω_p to the left of the light line (Fig. 1b) refers to the radiative plasmon. The non-radiative ω_s otherwise sits to the right of the light line and displays the characteristic asymptotic dispersion [5, 15]. Figure 1c is the energy-filtered imaging of the transmitted diffraction spot with the energy-selection window of 2 eV centered at the ω_s of ∼7 eV for unveiling the characteristic scattering in q space (k_x and k_y, the arbitrary in-plane q vectors), and unambiguously reveals the light cone (the white circle, Fig. 1c) with vanishing spectral intensities inside by the non-radiative nature of the ω_s in Fig. 1b. Instead, the ω_p counterpart in Fig. 1d shows noticeable spectral intensities both inside and outside the light cone, consistent with the observed crossover from the radiative to non-radiative ω_p upon increasing q in Fig. 1b [15]. In this small-q regime close to the light line (Fig. 1b), the quadratic q^2-dispersion of ω_p in Eq. (4) is, however, not obvious. We address the large-q plasmon dispersions in Figs. 2 and 3.

Figure 2a shows the unveiling of the first Brillouin zone in Si along the [1−10] projection, indicating the high-symmetry directions of ΓX, ΓL and ΓQ. We conduct the q-EELS probing of the plasmon involving dynamical oscillations of the valence electrons below the Fermi level along ΓL, which is of 0.95 Å^{-1} in the q-space length scale, and the q resolution of 0.1 Å^{-1} is employed. Figure 2b exhibits the q-EELS spectra of the dispersing plasmon from 16.6 eV at q = 0.1 Å^{-1} to 19.12 eV around the L point (∼1.0 Å^{-1}). Figure 2c manifests the $\omega-q$ map presentation of the spectra in Fig. 2b and the black dots are the pseudo-Voigt fitted plasmon peaks at designated q's. In accordance with Eq. (3), the plasmon peaks in Fig. 2c are recast into ω^2 in dependence of q^2 as shown in Fig. 2d, which unveils an unambiguous linearity in ω^2-q^2 in profound agreement with the FEG context, and the corresponding slope A readily represents the experimental measure of $\frac{3}{5}v_F^2$ [6]. One can then exploit Eq. (5) for n and also the subsequent derivation of m^*, and v_F provided ε_∞ is known [6]. The evaluation of ε_∞ has been a subtlety for decades [5, 8], whereas we have established that the Drude-Lorentz analysis of complex ε ($\varepsilon=\varepsilon_1+i\varepsilon_2$; Eq. (6) below) is, in effect, a solution for ε_∞ [6] considering the pertinent electronic screening would manifest itself by the appearance of an absorptive ε_2 peak (namely, the Lorentz term) above the Drude-like plasmon excitation upon $\varepsilon_1=0$ and vanishing ε_2 [5, 25].

$$\varepsilon(\omega)=1-\frac{\omega_D^2}{\omega^2+i\gamma_D\omega}-\frac{\omega_T^2}{\omega^2-\omega_T^2+i\gamma_T\omega}, \qquad (6)$$

where the second term on the right is the Drude component (ω_D) with the damping constant γ_D and the third term is the Lorentz component (ω_T) with the characteristic damping of γ_T [6].

Figure 2e shows the reported real-ε_1 (dark-green dots) and imaginary-ε_2 (light-green dots) parts of the ε around the experimentally observed plasmon onset in Si at 16.6 eV [26], superimposed with the Drude-Lorentz fitted complex dielectric function (dark- and light-gray curves). Notably, the demonstrated capturing of the reported ε in Fig. 2e exploits a single Drude component in Eq. (6) with $\omega_D=16.6$ eV and $\gamma_D=5$ eV, and further incorporations of Lorentz terms to depict the broad absorptive maxima in ε_2 at 10.5 and 14.5 eV rather deteriorate the agreement with the reported ε [6].

Considering the fundamental ω_p scaling with $\sqrt{\frac{1}{\varepsilon_\infty}}$, the ε_∞ can then be estimated by $\varepsilon_\infty=\left(\frac{\omega_D}{\omega_p}\right)^2$ [6], which leads characteristically to 1 in Si with $\omega_p=\omega_D=16.6$ eV. In principle, the lower bound of ε_∞ is unity like the vacuum and denotes the null screening by the absence of neighboring ε_2 peaks above the ω_p at 16.6 eV, indeed observed in Si (Fig. 2e) [6]. In addition, the consideration of $\varepsilon_\infty<1$ for the case of the observed plasmon above the nominal ω_p [27] is at odds with the principle of ε_∞ and the associated q-EELS derivations of n, m^* and v_F would lead to inconsistent results, for which it should be avoided and our q-EELS methodology becomes inapplicable.

Using $\varepsilon_\infty=1$, the A in Fig. 2d, and Eq. (5), we obtain the n, m^* and v_F of Si in Table 1 and the nominal values are given for comparisons. The q-EELS derived n and m^* are found to be higher than the nominal ones and this feature is associated with the inherent single-particle charge donation by the broad absorptive ε_2 maxima at 10.5 and 14.5 eV despite their irrelevance in the Drude-Lorentz fitting (Fig. 2e). Such

absorptive maxima below the plasmon would typically result in a higher n than the nominal value [5] and the concomitant conservation of $\varepsilon_\infty = 1$ is to be leveraged by an increase in m^* as evaluated in Table 1. To verify the consistency of these q-EELS elaborated n, m^* and v_F (Table 1), we use Eq. (4) to calculate the corresponding plasmon-dispersion curve (black curve, Fig. 2c) along with the single-particle continuum (white curve; $\frac{\hbar^2(q^2+2qk_F)}{2m^*}$), beyond which the plasmon should damp into electron-hole pairs [5, 6, 8]. Notably, the calculated dispersion (black curve, Fig. 2c) elegantly delineates the experiment (black dots), suggesting that the difference in the nominal and experimental n, m and v_F in Table 1 is within the systematic tolerable errors of our quantitative q-EELS methodology [6]. Figure 2f exhibits the further calculated q-dependent phase (v_ϕ; $\frac{\omega}{q}$) and group (v_g; $\frac{\partial\omega}{\partial q}$) velocities of the moving plasmon derived from Eq. (4) and normalized to the q-EELS evaluated v_F in Table 1 (light- and dark-green lines; dots, the experimental v_g), showing the characteristic divergence of v_ϕ in the long-wavelength limit of vanishing q and the iconic speeding up of v_g upon increasing q [8].

Figure 3a shows the first Brillouin zone of FeGe along the [001] projection and the room-temperature phase of this material features the simultaneous presence of the Dirac node, van Hove singularity and flat band in the valence band below the Fermi level [20-23], the latter two of which are characteristic of a local band flatness with a concomitantly elevated band mass in m^* [6] and refer to the emergence of electronic correlated phenomena such as charge-density waves [20-23]. The q-EELS probing of the plasmon dispersion of the valence electrons in FeGe shall, therefore, reveal an increased m^*.

Figure 3b and c exhibits the q-EELS spectra acquired along respective ΓK (0.84 $Å^{-1}$, length in reciprocal space) and ΓM (0.73 $Å^{-1}$). A compromised q resolution of 0.12 $Å^{-1}$ is adopted to gain the weak spectral intensity at large q. Figure 3e and f are the respective $\omega - q$ mapping of Fig. 3b and c. The plasmons along ΓK and ΓM are highly similar and both weakly dispersive (Fig. 3e and f). Moreover, the plasmon excitation at 19.5 (19.3) eV at 0.12 $Å^{-1}$ along ΓK (ΓM) is surprisingly inferior to the nominal 23.8 eV calculated by the nominal n_0 of $4.1 \times 10^{23}\,cm^{-3}$ (Table 1), m^* of m_0 (Table 1) and $\varepsilon_\infty = 1$ that is associated with the absence of screening interband transitions above the plasmon up to ~30 eV (Fig. 3b and c). Distinctly, the theoretical dispersions based on the n_0, m_0 and $\varepsilon_\infty = 1$ in Fig. 3e and f (white curves) deviate from the experiments (gray dots, Fig. 3e; black dots, Fig. 3f). To disentangle the underlying physics in these discrepancies (Fig. 3e and f), the experimental plasmon dispersions are scaled by $\omega^2 - q^2$ in Fig. 3h, where the corresponding linearity indicates the robust FEG character of the valence electrons along ΓK and ΓM despite certain electronic correlations imposed by the van Hove singularity and flat band [20-23]. The discrepancies are clearly not the result of deviations from the FEG behavior [5, 6, 8], and the possible effect of interband transitions, if any, above 30 eV would barely affect the distant plasmon at ~19 eV from the Drude-Lorentz analysis aspect [6]. Table 1 shows the readily evaluated n, m^* and v_F, indicating the electronic isotropy along ΓK and ΓM. Remarkably, the n is consistent with the n_0, unraveling that all valence electrons including the massless Dirac fermions tied to the Dirac cone (though very low in density due to the linearly-dispersing band character [6]) participate in the collective plasmon motion [9]. The m^* is indeed appreciable as expected and the calculated plasmon dispersion (gray curve, Fig. 3e; black curve, Fig. 3f) using the q-EELS derived v_F and $\hbar\omega_p$ in Table 1 well agrees with the experiments. The single-particle continuum (orange curve, Fig. 3e and f) is far below the experimental plasmon dispersion, suggesting that the observed plasmon broadening upon increasing q (Fig. 3b and c) shall arise from origins other than the electron-hole damping such as the electron-electron scattering, electron-phonon scattering, or defects [5]. In other words, the appreciable m^* of valence electrons derived from the q-EELS along ΓK and ΓM is entangled with the unique electronic band structure of FeGe and accounts for the observed discrepancies in the nominal, experimental ω_p and pertinent dispersions in Fig. 3e and f. Further q-EELS experiments along the out-of-plane ΓA direction in Fig. 3d and g indicates the robustness of the FEG context (Fig. 3h) and the even more elevated m^* of ~2.46 m_0 (Table 1) sheds light on the electronic anisotropy along this direction perpendicular to the basal plane. In Table 1, the comparable n of FeGe along ΓK, ΓM and ΓA to the nominal one casts similar k_F throughout and the elevated m^* along the three directions then mediates the slower v_F ($v_F = \frac{\hbar k_F}{m^*}$), which represents the single-particle electron velocity in maximum [8]. In Si, the slower v_F and larger k_F of the valence electrons (Table 1) are within the precision tolerance of ±10% and not to be further interpreted.

Concluding remarks

On the basis of the plasmon-dispersion physics in solids of a FEG character, we introduce the q-EELS methodology for m^* and v_F (eventually also n) [5, 8, 9] and formulate the explicit analytical equations for these electronic parameters [6]. The capability of this q-EELS methodology for m^* and v_F is demonstrated using the plasmon dispersions in Si and FeGe up to the Brillouin-zone boundaries, with the Si exemplifying a compromised precision by the characteristic electronic absorption below the plasmon excitation and the FeGe illustrating an elevated m^* due to the iconic electronic band structure decorated by the van Hove singularity and flat band [20-23]. The q-EELS technique for the plasmon dispersion close to the light line is also manifested using Al. This work provides an overall scope on the q-EELS probing of plasmon dispersions and its emergent applications in deriving m^* and v_F, which has not been reported until recently [6] and opens up vast opportunities for quantitative q-EELS studies of materials.

Author contributions

Chih-Ying Huang, Somboon Fongchaiya and Chen-Yu Hung conducted the q-EELS experiments and quantitative evaluations of the electronic parameters. Ta-Lei Chou, Ssu-Yen Huang, Chao-Sung Lin and Chun-Wei Chen supervised the work. Mason Klemm, Sijie Xu, Bin Gao and Pengcheng Dai grew the FeGe single crystals. Ming-Wen Chu wrote the manuscript and interpreted all results.

Funding

National Science and Technology Council (Grant No. 109-2628-M-002-0054-MY3, 110-2112-M-032-014-MY3, 112-2124-M-006-009, 113-2124-M-006-011, 113-2112-

M-032-013, 113-2119-M-002-025 and 114-2124-M-002-015); National Taiwan University, Academia Sinica (Grant No. AS-iMATE-113-12 and AS-iMATE-113-15); and Ministry of Education. The single-crystal synthesis and characterization at Rice are supported by U.S. National Science Foundation (DMR-2401084); and the Robert A. Welch Foundation (Grant No. C-1839 to P.D.).

Conflicts of interest

None declared.

References

1. Husain A A, Huang E W, Mitrano M, Rak M S, Rubeck S I, Guo X, Yang H, Sow C, Maeno Y, Uchoa B, Chiang T C, Batson P E, Phillips P W, and Abbamonte P (2023) Pine's demon observed as a 3D acoustic plasmon in Sr_2RuO_4. *Nature* 621: 66–70.
2. Lin Z, Wang C, Balassis A, Echeverry J P, Vasenko A S, Silkin V M, Chulkov E V, Shi Y, Zhang J, Guo J, and Zhu X (2022) Dramatic plasmon response to the charge-density-wave gap development in 1T-$TiSe_2$. *Phys. Rev. Lett.* 129: 187601.
3. Politano A, Chiarello G, Ghosh B, Sadhukhan K, Kuo C -N, Lue C S, Pellegrini V, and Agarwal A (2018) 3D Dirac plasmons in the type-II Dirac semimetal $PtTe_2$. *Phys. Rev. Lett.* 121: 086804.
4. Mendis B G (2022) Quantum theory of magnon excitation by high energy electron beams. *Ultramicroscopy* 239: 113548.
5. Raether H (1980) *Excitation of plasmons and interband transitions by electrons*, (Springer-Verlag, Berlin, Heidelberg, New York).
6. Wang I-T, Chou T-L, Hsu C-E, Lei Z, Wang L-M, Lin P-H, Luo C-W, Chen C-W, Kuo C-N, Lue C S, Chen C H, Hsueh H-C, and Chu M-W (2024) The growing charge-density-wave order in CuTe lightens and speeds up electrons. *Nat. Commun.* 15: 9345.
7. Qi R, Shi R, Li Y, Sun Y, Wu M, Li N, Du J, Liu K, Chen C, Chen J, Wang F, Yu D, Wang E-G, and Gao P (2021) Measuring phonon dispersion at an interface. *Nature* 599: 399–403.
8. Platzman P M, and Wolff P A (1973) *Waves and interactions in solid state plasma*, (Academic Press, New York, London).
9. Pines D, and Bohm D (1952) A collective description of electron interactions: II. collective vs individual particle aspects of the interactions. *Phys. Rev.* 85: 338–353.
10. Schmüser P (1964) Anregung von volumen- und oberflächenplasmaschwingungen in Al und Mb durch mittelschnelle elektronen. *Z. Phys.* 180: 105–126.
11. Daniels J (1967) Energieverlustmessungen an silber mot hoher energieauflösung. *Z. Phys.* 203: 235–249.
12. Zeppenfeld K (1968) Anisotropy of plasmon oscillations in graphite. *Z. Phys.* 211: 391–399.
13. Kröger E (1968) Berechnung der energieverluste schneller elektronen in dünnen schichten MIT retardierung. *Z Physik.* 216: 115–135.
14. Chen C H, Silcox J, Garito A F, Heeger A J, and MacDiarmid A G (1976) Plasmon dispersion and anisotropy in polymeric sulfur nitride, $(SN)_x$. *Phys. Rev. Lett.* 36: 525–528.
15. Batson P E, Chen C H, and Silcox J (1976) Plasmon dispersion at large wave vectors in Al. *Phys. Rev. Lett.* 37: 937–940.
16. Pezzini S, van Delft M R, Schoop L M, Lotsch B V, Carrington A, Katsnelson M I, Hussey N E, and Wiedmann S (2018) Unconventional mass enhancement around the Dirac nodal loop in ZrSiS. *Nat. Phys.* 14: 178–183.
17. Shao Y, Rudenko A N, Hu J, Sun Z, Zhu Y, Moon S, Millis A J, Yuan S, Lichtenstein A I, Smirnov D, Mao Z Q, Katsnelson M I, and Basov D N (2020) Electronic correlations in nodal-line semimetals. *Nat. Phys.* 16: 636–641.
18. Liou S C, Shie C -S, Chen C H, Breitwieser R, Pai W W, Guo G Y, and Chu M -W (2015) π-plasmon dispersion in free-standing graphene by momentum-resolved electron energy-loss spectroscopy. *Phys. Rev. B* 91: 045418.
19. Midgley P A (1999) A simple new method to obtain high angular resolution -q patternsω. *Ultramicroscopy* 76: 91–96.
20. Teng X, Chen L, Ye F, Rosenberg E, Liu Z, Yin J-X, Jiang Y-X, Oh J S, Hasan M Z, Neubauer K J, Gao B, Xie Y, Hashimoto M, Lu D, Jozwiak C, Bostwick A, Rotenberg E, Birgeneau R J, Chu J-H, Yi M, and Dai P (2022) Discovery of charge density wave in a kagome lattice antiferromagnet. *Nature* 609: 490–495.
21. Teng X, Oh J S, Tan H, Chen L, Huang J, Gao B, Yin J -X, Chu J -H, Hashimoto M, Lu D, Jozwiak C, Bostwick A, Rotenberg E, Granroth G E, Yan B, Birgeneau R J, Dai P, and Yi M (2023) Magnetism and charge density wave order in kagome FeGe. *Nat. Phys.* 19: 814–822.
22. Klemm M L, Siddique S, Chang Y -C, Xu S, Xie Y, Legvold T, Kiani M T, Teng X, Gao B, Ye F, Cao H, Hao Y, Tian W, Luetkens H, Matsuda M, Natelson D, Guguchia Z, Huang C -L, Yi M, Cha J J, and Dai P (2025) Vacancy-induced suppression of charge density wave order and its impact on magnetic order in kagome antiferromagnet FeGe. *Nat. Commun.* 16: 3313.
23. Oh J S, Biswas A, Klemm M L, Tan H, Xie Y, Gao B, Hashimoto M, Lu D, Yan B, Dai P, Birgeneau R J, and Yi M (2025) Disentangling the intertwined orders in a magnetic kagome metal. *Sci. Adv.* 11: eadt2195.
24. Kenichi A (2019) *Quantum theory of electron in solids*, (University of Tokyo Press, Tokyo).
25. Cudazzo P, Gatti M, and Rubio A (2012) Plasmon dispersion in layered transition-metal dichalcogenides. *Phys. Rev. B* 86: 075121.
26. Palik E D (ed.) (1998) *Handbook of optical constants of solids*, (Academic Press, New York)
27. Liang W Y, and Cundy S L (1969) Electron energy loss studies of the transition metal dichalcogenides. *Phil. Mag.* 19: 1031–1043.

Microscopy, 2026, 75, 157–163
https://doi.org/10.1093/jmicro/dfag007
Special Issue Paper